Linewidth Broadening in Short-Wavelength Quantum Cascade Lasers

Andrzej Kolek[,1,*] Grzegorz Hałdaś[,1] Piotr Gutowski[,2] Grzegorz Sobczak[,2]
Dorota Pierścińska[,2] and Maciej Bugajski[2]

[1]*Department of Electronics Fundamentals, Rzeszów University of Technology, al. Powstańców Warszawy 12, Rzeszów 35-959, Poland*
[2]*Łukasiewicz Institute of Microelectronics and Photonics, al. Lotników 32/46, Warszawa 02-668, Poland*

Nonequilibrium Green's function modeling of the structure used for III-V quantum cascade lasers emitting at approximately 5-μm wavelength is performed to get insight into and analyze the processes that determine the linewidth of the optical (inter-sub-band) transition. Theoretical results are compared with electroluminescence data collected for real structures. Excellent agreement is found for both the transition energy of approximately 234 meV and the linewidth of approximately 32 meV, typical for this sort of device. Careful inspection of simulation data shows that, for these structures, the interface-roughness (IR) scattering contributes to the optical linewidth $\cong$ 50%. The decreased broadening due to IR scattering is not due to very smooth interfaces, but rather due to the finite carrier concentration and the decreased population of final states $\mathbf{k}'$ available for the initial state $\mathbf{k}$ in the limit of vanishing in-plane momentum $\mathbf{k} \to 0$. Further line narrowing is caused by nonparabolicity coupled with the highly nonthermal occupation of the lower laser sub-band, which destroys the population inversion for the hot carriers.

I. INTRODUCTION

In the last 20 years, quantum cascade lasers (QCLs) have developed greatly due to their high gain in a hardly accessible (in comparison with other types of devices) mid-infrared (MIR) or THz frequency range. The large optical gain of these devices arises due to the narrow linewidth of the laser transition. This feature follows from the QCL operation principle; lasing is due to the transitions between the sub-bands, which in contrast to interband processes preserve the same curvature of the dispersion relation. In such circumstances, the mentioned linewidth is almost exclusively described by the dephasing processes of the optical transition [1–3]. The dephasing is directly related to various scattering mechanisms that may broaden both the sub-bands and the inter-sub-band transitions [4]. In the case of MIR devices, utilizing transitions at approximately 10-μm wavelength, the main contribution to the laser linewidth comes from the intra-sub-band broadening of laser levels resulting from the *interface-roughness* (IR) scattering [5–9]. The THz devices, which utilize much wider wells, are much less sensitive to the fluctuations of the layer widths. Therefore, IR plays a lesser role, whereas the role of other scattering mechanisms is enhanced

[10]: impurity scattering and electron-electron scattering become the most relevant gain broadening mechanisms [11–14].

In short-wavelength ($\lambda \le 5 \ \mu$m) QCLs with extremely narrow wells, the number of interfaces per state involved in the lasing transition increases. Simultaneously, the sensitivity of the level energy to the fluctuations of the layer width increases. For both these reasons, the broadening of the laser transition due to the interface roughness is significantly enhanced; theoretically, widths as large as 170–330 meV were predicted [8]. At the same time, the experiments showed the broadening increased up to merely 40 meV [8,15,16], whereas most of the designs exhibit smaller linewidth in the range 25–30 meV [17–20]. This inconsistency was explained by the vertical correlation of the roughness potential between adjacent interfaces (SiGe devices) or assuming very smooth interfaces (III-V devices) [8]. In the following, we show that the linewidth of the order 30 meV, typical for short-wavelength QCLs, can be theoretically justified also when the vertical correlations between the roughness potentials are absent and/or the interfaces are not very smooth. Our main research tool is the theoretical analysis that uses the nonequilibrium Green's function formalism (NEGF) [21,22], which is known to catch best the physics of the structures that utilize both quantum and classical phenomena. This method

---

*akoleknd@prz.edu.pl

is especially relevant for the current case as it accounts for the nondiagonal dephasing [23]. It was shown that nondiagonal correlations between laser states lead to a reduction in the corresponding linewidth below the sum of the individual linewidth contributions [24,25]. This effect should be considered only within the fully quantum-mechanical approach, which correctly handles both the collisional broadening and the nondiagonal correlations [26]. Theoretical considerations are verified against experimental data gathered for the devices, which are grown for this purpose.

II. MODEL AND METHOD

A. Hamiltonian

As a QCL is a stratified *n*-type device, the one-band Hamiltonian parametrized for in-plane kinetic energy provides a good-enough description. The noninteracting Hamiltonian that accounts for band nonparabolicity reads [27,28]

$$H = \frac{-\hbar^2}{2} \frac{d}{dz} \frac{1}{m(E,z)} \frac{d}{dz} + V(z) + \frac{\hbar^2 k^2}{m(E,z)}, \quad (1)$$

where z is the coordinate in the growth direction, k is the in-plane momentum modulus, E and V are the total and potential energies, and other symbols have the usual meaning. The Hamiltonian H is used in the NEGF equations together with the set of self-energies related to various scattering processes.

B. Scattering self-energies

For the scattering on a rough interface, localized at $\langle z \rangle = z_{\text{int}}$ and characterized by two-dimensional (2D) potential with the rms height Δ and the correlation length Λ, the appropriate self-energy reads [28–30]

$$\Sigma_{\text{IR}}^{R,<}(z_{\text{int}}, z_{\text{int}}, k, E)$$
$$= \frac{\delta V^2}{4} \frac{\Lambda^2}{4\pi} \int q^2 \, dq \int_0^\pi d\Theta e^{-\Delta^2(k^2+q^2-2kq\cos\Theta)/4}$$
$$\times G^{R,<}(z_{\text{int}}, z_{\text{int}}, q, E), \quad (2)$$

where δV^2 is the conduction band offset at the interface, and $G^R, G^<$ are the retarded and lesser Green's functions (GFs), respectively. Equation (2) is formulated in a position representation with δ functions as the basis vectors. In numerical approaches, a discrete mesh is used. In the case of rectangular-shaped base vectors, $\phi_i \sim \{\Theta(z - [z_i + z_{i-1}]/2) - \Theta(z - [z_i + z_{i+1}]/2)\}$, where Θ is the Heaviside function, the normalization condition requires $\langle \phi_i \phi_i^* \rangle = 1/\delta z_i$, where $\delta z_i = (z_{i+1} - z_{i-1})/2$ is the mesh eye attributed to the site i at z_i. In such an implementation, the matrix element of the interface-roughness scattering potential becomes $\langle V_{\text{IR}} \rangle = \langle \phi_i | V_{\text{IR}} | \phi_i^* \rangle = \delta V \Delta / \delta z_i$, and the factor δV^2 in Eq. (2) changes to $(\delta V \Delta / \delta z_i)^2$. This formulation is different from that in Refs. [28,30], which uses the scaling $\delta V^2 \Delta / \delta z_i$. However, our observation is that only with our approach the response is independent of the mesh size. Moreover, the proposed scaling restores proportionality to Δ^2, valid for the eigenstate basis (both in NEGF [31–33] and semiclassical approaches [4,34]). In the case, when the discretization points z_i do not exactly hit the interface position, i.e., $z_{\text{int}} \neq z_i$, the reasonable approximation is to distribute Σ_{IR} between the points z_i, z_{i+1}, adjacent to the interface (proportionally to $|z_{i,i+1} - z_{\text{int}}|/|z_{i+1} - z_j|$), and the approximate GF at the interface with the GF at the respective grid points [28–30]. This approximation works well when the wave functions penetrate the barrier material. For tall and wide barriers, the approximation underestimates the IR scattering as the part of the self-energy assigned to a node located in a barrier material is probed by the negligibly small value of the GF.

Another self-energy of interest is due to the longitudinal polar optical (LO) phonons. For screened dispersionless phonons with energy $E_{\text{LO}} = \hbar \omega_{\text{LO}}$, the retarded LO-phonon self-energy reads [29]

$$\Sigma_{\text{LO}}^R(z, z', k, E) = \frac{\beta}{2\pi^2} \int q dq I(|z - z'|, k, q)[(n_B + 1)G^R(z, z', q, E - E_{\text{LO}}) + n_B G^R(z, z', q, E + E_{\text{LO}})$$
$$+ \frac{1}{2} G^<(z, z', q, E - E_{\text{LO}}) - \frac{1}{2} G^<(z, z', q, E + E_{\text{LO}})], \quad (3a)$$

where $\beta = e^2 E_{\text{LO}}(\varepsilon_\infty^{-1} - \varepsilon_0^{-1})/2$,

$$I(|z - z'|, k, q) = \int_0^{\pi/a} dq_z \frac{\cos(q_z|z - z'|)}{\sqrt{(q_z^2 + l^2)^2 - 4k^2q^2}} \left(1 - \frac{q_0^2(q_z^2 + l^2)}{(q_z^2 + l^2)^2 - 4k^2q^2}\right), l^2 = q_0^2 + k^2 + q^2, \quad (3b)$$

$n_B = [\exp(E_{LO}/k_B T) - 1]^{-1}$ is the phonon occupation number, and q_0 is the inverse screening length. As opposed to Σ_{IR}, the LO-phonon self-energy is a nonlocal perturbation.

C. Optical broadening

Data presented in Fig. 1 refer to the structure considered in the seminal papers on inter-sub-band absorption linewidth [6,7]: the linewidths due to the IR and the LO-phonon scatterings are calculated for 8-nm-wide GaAs quantum well as a function of the in-plane energy, $E_k = \hbar^2 k^2 / 2 m_{||}$. For the reasons discussed above, the height and the width of the confining barriers are decreased to 0.4 eV and 3 nm so that the partitioning of the IR self-energy over the nodes on both sides of the interface provides a reasonable approximation.

For large momenta, the IR broadening fits exactly the microscopic theory of Ando [7]. A deviation observed for the small in-plane energies occurs since particles with $k \approx 0$ can be scattered only to states with lower potential energy. The average state energy is then lowered (see Fig. 1 inset) as well as the linewidth (approximately by a factor of 2) because only the positive shoulder (i.e., for $k' > k = 0$) of the line spectrum is accessible for the scattered carriers.

FIG. 2. FWHM of the absorption peak calculated with NEGF method for the 8-nm quantum well as a function of the parameter Δ at fixed $T = 400$ K. The slope of the approximating line is 40 meV/nm^2. The upper line is the plot of Eq. (4). Details of the calculations are provided in the caption of Fig. 1.

Some discrepancy with Ando's theory can be observed also for LO-phonon broadening: the step at $E_k = E_{LO}$ is not present; however, the average value of $\Gamma \approx 2$ meV agrees well with this theory (see Fig. 4 in Ref. [7]). One can further observe that there is a negative correlation between IR and LO-phonon scattering mechanisms, which at small E_k's makes the impact of coexistent interactions smaller than the sum of individual impacts. Data in Fig. 2 demonstrate that, in spite of this correlation, the quadratic dependence on the parameter Δ is preserved. However, the slope $\cong 0.04$ eV/nm^2, found in this dependence, is much lower than the value 0.21 eV/nm^2 predicted by the relation

$$\Gamma = \frac{\pi m}{\hbar^2} \Delta^2 \Lambda^2 (F_{11} - F_{00})^2, \qquad (4)$$

provided in Ref. [8]. This relation is valid for negligible carrier concentration. In such a case, only the states at the bottom of the sub-bands are occupied so that the total
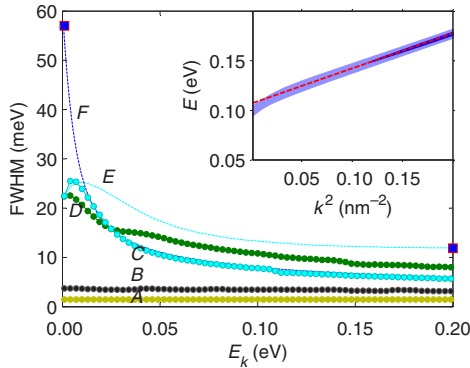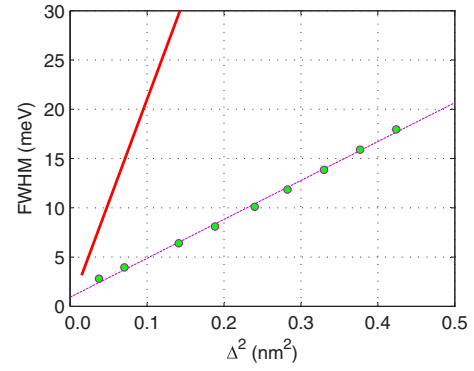

FIG. 1. The full width at half maximum (FWHM) of the absorption line calculated with NEGF method for the 8-nm quantum well confined with 3-nm-thick and 0.4-eV-tall barriers. Calculations are done for fully parabolic in-plane energy, i.e., assuming $m(E,z) = m_{||} = 0.108$ in the last term in Eq. (1). Lines with symbols refer to the transitions at energy E_k and the following self-energies included into formalism: A: none, B: Σ_{LO} (400 K, Debye screening length $1/q_0 = 7.12$ nm), C: $\Sigma_{IR}(\Lambda = 9$ nm, $\Delta = 0.53$ nm), D: $\Sigma_{IR} + \Sigma_{LO}$. Line E is for case C but refers to all transitions in the range 0–E_k; the value of FWHM, $\Gamma = 11.85$ meV at maximum E_k (square) is the estimate of the total FWHM calculated with the NEGF method. Line F is the theoretical dependence of IR–intra-sub-band linewidth calculated according to Ando's theory [e.g., Ref. [7], Eq. (23)]; the value $\Gamma = 58$ meV at $E_k = 0$ (square) is the estimate of the total FWHM given by Eq. (4). Inset: dispersion relation of the upper level of the optical transition doublet.
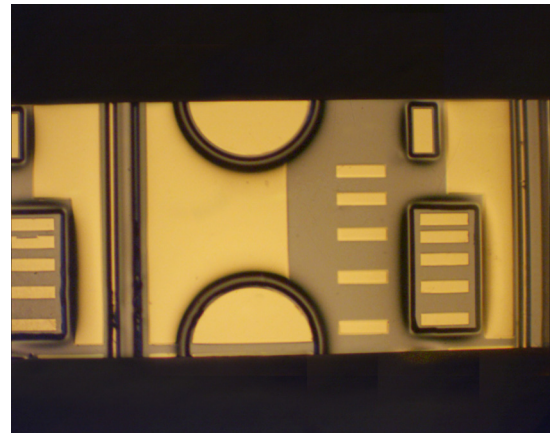

FIG. 3. Test structures for electroluminescence and contact resistance measurements.

FWHM equals FWHM at $E_k = 0$ (see Fig. 1). The reduced linewidths of the transitions at small E_k's, discussed above, would then give the value $\Gamma(E_k = 0) \approx 22$ meV. In the analyzed quantum well, the Fermi level is located at $E_k \cong 26$ meV, so there is a finite carrier concentration, which allows for the transitions at $E_k > 0$. They contribute to the linewidth, making it initially increase but eventually be dumped to the value 11.85 meV, which is almost 5 times smaller than the value predicted by Eq. (4). These numbers illustrate how much the linewidth of doped structures can differ from the rough theoretical estimate.

Obviously, different pictures can be obtained depending on the structure geometry, temperature, and doping (which determine the occupation of the states and dynamic screening) and the IR-scattering parameters. However, the case being analyzed seems to be relevant for the quantum cascade lasers to which the paper is addressed. Namely, (i) the IR roughness correlation length in the range 6 nm $< \Lambda < 20$ nm is commonly reported for this type of device (see Ref. [35] for discussion), (ii) the temperature 400 K is higher than the ambient temperature at which the short-wavelength QCL can successfully operate; however, in this type of device, the population of overheated electrons occupying laser sub-bands is highly nonthermal [36,37] so that the electron temperature of the order 400–700 K is quite common [38], (iii) the emission wavelength takes the value of several dozen tens of meV so that the inter-sub-band contribution Γ_{inter} to IR broadening is quite minor, (iv) the roughness rms height of $\Delta \approx 0.5 - 1$ monolayer width ($a = 0.28$ nm) is physically best justified and experimentally verified. However, in QCL, many interfaces perturb the laser states. As each of them adds the factor proportional to $\Delta |\zeta(z_{\text{int}})|^2$ to the linewidth, the multiple contributions can be modeled by larger values of Δ.

III. GAIN BROADENING IN SHORT-WAVELENGTH QCL

A. Devices and experiment

The devices used in this study are the strain-compensated $In_{0.66}Ga_{0.34}As/In_{0.346}Al_{0.654}As$ QCLs emitting at approximately 5.25 μm, grown by solid-source molecular beam epitaxy (MBE) technology [39]. The active region, originally designed by Evans *et al.* [40], is of four-well two-phonon resonance design; the layer sequence of one period of the structure, starting from the injection barrier, is **2.8**, 1.36, **1.14**, 4.75, **1.14**, 4.18, **1.23**, 4.02, **2.02**, 3.02, **1.44**, 2.71, **1.52**, 2.41, **1.6**, 2.3, **1.76**, 2.19, **1.76**, 1.95, **2.03**, 1.95 nm. The $In_{0.346}Al_{0.654}As$ layers are denoted in bold, and $In_{0.66}Ga_{0.34}As$ layers are denoted in normal font. The underlined layers are n doped to 2×10^{17} cm^{-3}. The core region containing 30 repetitions of the basic module is sandwiched between two 500-nm-thick lattice-matched $In_{0.53}Ga_{0.47}As$ layers, which are n doped to 4×10^{16} cm^{-3}. The low-doped, $n = 2 \times 10^{17}$ cm^{-3}, InP

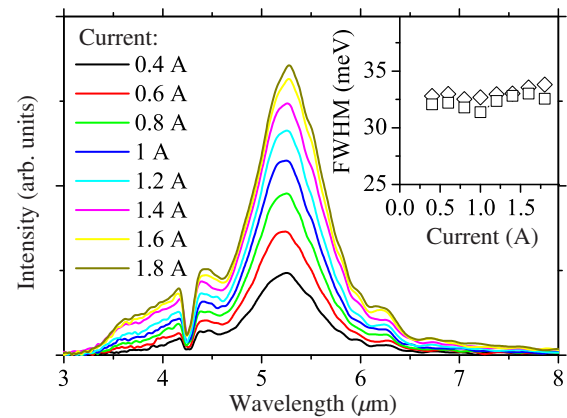FIG. 4. Electroluminescence spectrum of the QCL structure (wafer no. C1003) measured as a function of the bias current at the temperature 15 °C. Inset: FWHM of the spectra estimated with a two-parameter (height, width) Gaussian fit of the experimental data for two samples from different wafers: no. C1003, no. C1080 grown according to the same recipe.

substrate is used as the bottom waveguide layer; the upper waveguide layer is formed by 2.5-μm-thick $In_{0.52}Al_{0.48}As$, doped to $n = 1 \times 10^{17}$ cm^{-3}, lattice matched to InP. The whole structure is followed by 500-nm-thick $n^+ = 8 \times 10^{18}$ cm^{-3} $In_{0.53}Ga_{0.47}As$ cap layer.

Part of each wafer is devoted to the test structures shown in Fig. 3. Electroluminescence (EL) structures are lithographically patterned 500-μm-diameter circles, etched into mesas using HBr:HNO3:H2O (1:1:10) wet chemical solution. The etching goes through the epitaxially grown material. A second lithography step is used to apply the top contact metallization. The contacts consist of 150 Å Ti followed by 2500 Å Au and are alloyed at 370 °C for 60 s. The mesas are cleaved into semicircular structures and tested on the probe stage.

The electroluminescence is measured at 15 °C as a function of the bias current. Current pulses with widths of 400 ns and 100-kHz repetition are applied. The emission from the devices is collected by an off-axis parabolic mirror and sent into a Fourier-transform infrared spectrometer (FTIR) operated in a step-scan mode. The liquid-nitrogen-cooled MCT detector is used to measure the emission intensity. Results are presented in Fig. 4. The main peak of the EL spectrum corresponds to the lasing transition. The origin of the broad peak located in between 3–5 μm is unknown. An atmospheric CO_2 absorption dip can be seen near 4.23 μm [41]. Spectra are not corrected for detector responsivity.

The inset in Fig. 4 shows the EL FWHM as a function of the current density. The FWHM is estimated fitting Gaussian curves to the experimental data. Contrary to what is observed for QCL devices emitting at approximately 10-μm wavelength [9,41], there is no systematic dependence of EL width on the injection current. It rather seems to hardly depend on the current. The average width

of approximately 32 meV, which is 14% of the peak emission energy, corresponds well with the estimates reported for other devices emitting at approximately 5-μm wavelength [8,15–20,41].

B. Theoretical analysis

1. Computational details

To identify the gain broadening mechanisms in a real QCL, a more detailed model than the one presented in Sec. II is needed. Apart from IR and LO-phonon, other scattering mechanisms should be considered. Fortunately, their contribution to line broadening was shown to be small [7]. On the other hand, the scattering processes influence the electronic transport and so, indirectly, the FWHM of the optical gain spectrum. One possibility of such mediating influence is the occupation of the laser sub-bands, which depends on the transport, and simultaneously, as shown in Fig. 1, can influence the total linewidth through the energy dependence of the linewidths for the transitions at different k's. Therefore, more self-energies, related to other scattering mechanisms, need to be included into NEGF formalism. The scatterings from ionized impurities and alloy disorder are implemented in a way described in Ref. [29]. For the scattering from acoustic phonons, the energy-averaged approximation of Ref. [28] is adapted. The electron-electron interactions are treated within the mean-field approximation by solving the Poisson equation self-consistently with the NEGF equations. The boundary conditions imposed onto the Poisson equation ensure device neutrality. The equations of the NEGF formalism are applied to the Hamiltonian of Eq. (1) in which the potential V is the sum of the Hartree potential and the conduction-band-edge energy, E_c. For short-wavelength devices, accounting for nonparabolicity is a must. In Eq. (1), it is realized assuming energy-dependent effective mass [42]

$$m(E,z) = m^*(z)\{1 + [E - E_c(z)]/E_g(z)\}, \qquad (5)$$

where E_g is the band-gap energy. It was shown that such an approach gives results that very well match the results obtained with the eight-band kp model [27].

All calculations are done in the real space (position basis) assuming rectangular-shaped base vectors in the z direction. Nonuniform discretization mesh is used to reduce the numerical load without losing the accuracy [43]. Due to the periodicity of QCL structures, the range of analysis is limited to slightly more than one QCL module (period) and the remaining part of the cascade is mimicked by suitable contact self-energies [28,44,45]. The parameters m^* and E_g for ternary materials of QCL layers are taken from Ref. [46], which uses the tight binding sp3d5s* model for band-structure calculations. Conduction band-gap offsets are calculated using the model solid theory including strain [47] for which the material parameters

TABLE I. Parameters used in NEGF modeling of short-wavelength QCL structure.

	Well	Barrier
	In$_{0.6}$Ga$_{0.4}$As	Al$_{0.56}$In$_{0.44}$As
m^*	0.045	0.091
E_g (eV)	0.84	1.84
Alloy matrix element (eV)	0.49 [49]	0.47 [50]
ΔE_c (eV)	0.825	
n_{dop} (cm^{-3})	2×10^{17}	
LO-phonon energy (eV)	0.032	
Deformation potential (eV)	5.89	
Density (kg/m^3)	5590	
Sound velocity (m/s)	4810	
$\varepsilon/\varepsilon_\infty$	13.73/11.36	
Δz_{max}(nm) [43]	0.8	
Temperature (K)	288	
Screening length, λ_{Debye} (nm)	24	
Scattering time in the leads, τ_{lead} (ps) [28]	0.1	
Number of QCL periods, N_{per}	30	

are taken from Ref. [48]. The parameters for alloy disorder scattering are adopted from Refs. [49] and [50]. All values of material, physical, and model parameters used in the calculations are listed in Table I.

The NEGF-Poisson equations are iterated until the self-consistent Born solution is obtained. The convergence criteria used to stop the iterations are the same as in Ref. [44], except for the case of the quantum well considered in Sec. II C for which the Poisson equation is not included. In that case, the condition for charge neutrality is not imposed [51].

The linear response (small signal) gain or absorption are calculated based on the *full theory* outlined in Ref. [23], adapted for the case of energy-dependent effective mass [52]. This is a perturbation theory that requires only the steady-state solution of the system, not interacting with the optical field, so that looking for the time-dependent solution of the interacting system is not necessary, which greatly saves computational time and memory resources [53]. As stressed in Ref. [24], the use of the *full theory*, which accounts for the fluctuations $\delta\Sigma$ of the self-energies caused by the optical field, is crucial for the correct treatment of the nondiagonal scatterings.

2. Results

Results of the calculations are presented in Figs. 5–8. As discussed in Sec. II C, the reasonable value of the correlation length of IR potential is $\Lambda = 9$ nm. This value is fixed in the calculations in contrast to the rms height Δ of IR potential, which is treated as a fitting parameter. Results of such calculations are shown in the inset of Fig. 6. The best fit of the calculated gain with the EL experiment is found for $\Delta = 0.53$ nm, which is a bit smaller than one lattice
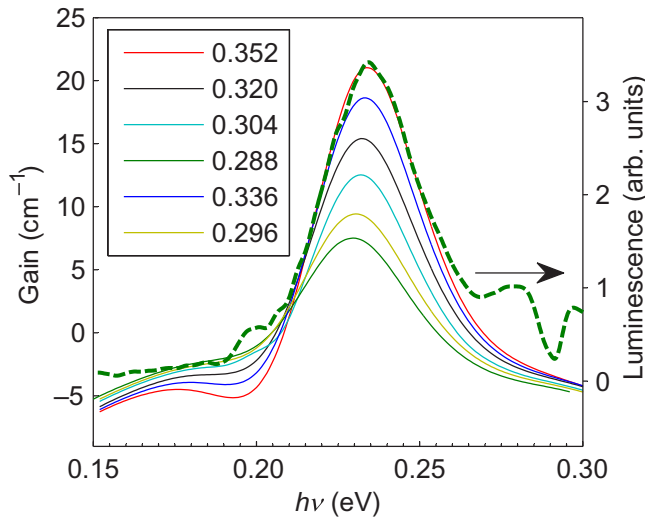
FIG. 5. Gain spectrum calculated with the NEGF method for different bias voltage per module (solid lines, left axis) compared to the measured electroluminescence for the bias current 1.8 A (dashed line, right axis).

spacing. As shown in Fig. 5, the calculated gain spectrum fits very well the measured EL. Whereas the width of the calculated spectrum can be tuned by the value of the parameter Δ, the position of the peak cannot. The excellent agreement of the calculated and the measured values of the transition energy, $E_\nu = h\nu \approx 234$ meV, confirms the proper choice of the remaining parameters used in the theoretical model.
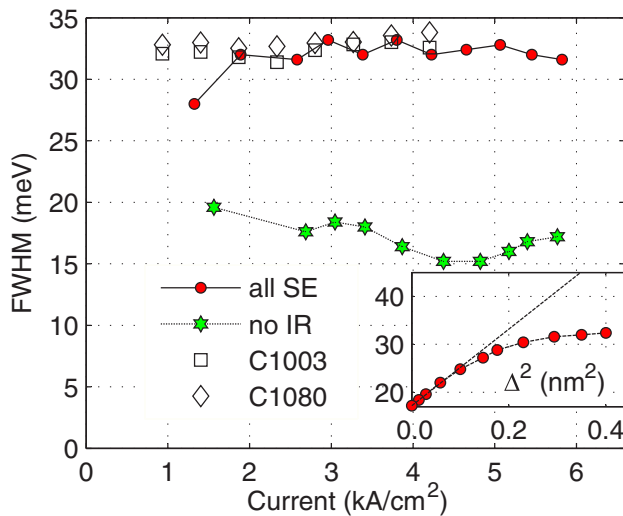

FIG. 6. FWHM of the gain spectrum calculated with the NEGF method (filled circles) compared to the measured FWHM of electroluminescence (hollow symbols) versus the bias current. The components of the calculated quantity are also shown, i.e., FWHM with all but IR self-energy (stars) included in the calculations. Inset: FWHM as a function of parameter Δ.
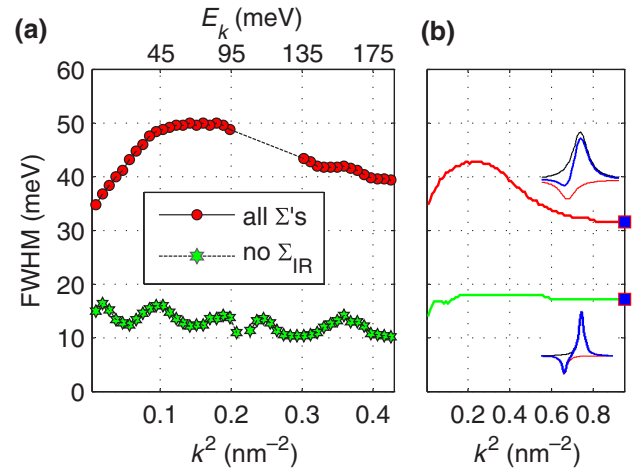

FIG. 7. (a) Linewidth of the optical transition occurring at k^2 (in-plane momentum modulus squared) calculated for the bias $U = 352$ mV/module (5.8 kA/cm²) for the case when all (circles) or all but IR (stars) scatterings are active. (b) FWHM of the cumulative gain, which comprises all transitions in the range 0–k^2; the values for the total gain are reached at maximum k^2 (squares). Insets: the spectra of gain (black), absorption (red), and total gain (blue) for the cases of broad (upper inset) and narrow (lower inset) linewidths of the optical transitions.

The most valuable result is presented in Fig. 6, in which the FWHM of the calculated gain spectrum is compared with the FWHM of the measured EL. Once again, an excellent agreement is observed. It is then interesting to examine the contributions to the gain linewidth due to different scattering mechanisms. They can be obtained excluding the respective Σs from the calculations. In some cases, such an exclusion changes not only the gain spectrum, but also the device operating point, so that
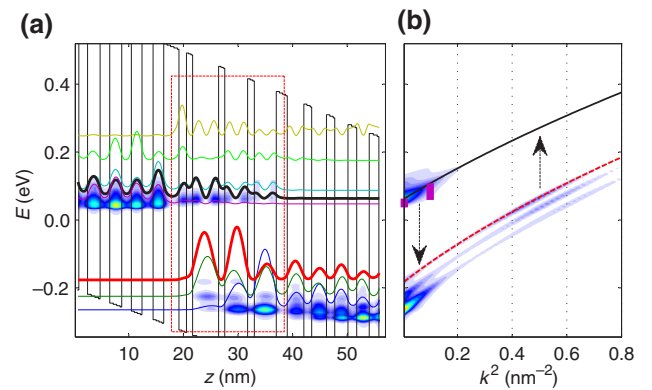
FIG. 8. Density of electrons (DOEs) calculated with the NEGF method with all scattering self-energies taken into account (color maps). In (a), the position-resolved DOEs is shown for the vanishing in-plane momentum ($k = 0$). In (b), the k-resolved DOEs averaged over the active region [red box in (a)] is shown. Lines show the squared eigenfunctions of the major laser states in (a) or the dispersion relations of the laser sub-bands in (b).

the full self-consistent solution is necessary for each set of the self-energies included in the NEGF calculations. The exclusion of IR scattering narrows the gain spectrum (decreases its FWHM) by approximately 50%. This number illustrates how much the performance of the device can increase when its technology is raised to the level enabling the growth of ideally smooth interfaces. Indeed, short-wavelength devices with the FWHM of the luminescence spectrum as low as 25–30 meV at 300 K have been demonstrated [17–20], which indicates the excellent crystalline and interface quality of the materials grown in these labs.

On the other hand, this number reveals that, in this kind of device, *the contribution of IR scattering to the line-broadening mechanism is lower than expected*. Another observation is that our *estimate of the parameter Δ is considerably larger than the value 0.1 nm* reported in the number of studies on this kind of device [27,54,55].

3. Discussion

The findings of the previous paragraph can be explained as follows:

1. The estimates of the roughness height Δ, reported in the literature, were obtained in a way very similar to ours, i.e., fitting the theory to the experiment. The applied theory [8] assumes negligible carrier concentration, which, as shown in Sec. II C, provides values an order of magnitude larger than the NEGF method. Small Δ's are then necessary to compensate this effect, which postulates very smooth interfaces. Our approach is not limited to low carrier concentrations, so the estimated widths are more precise. The meaning of our result is that $\Gamma \cong 30$ meV is well justified also when the interfaces are not so smooth.

2. The contribution of IR scattering to the optical linewidth is further decreased due to two more reasons: (i) the decreased IR broadening of the transitions occurring at the bottom of sub-bands (small in-plane momenta), (ii) nonparabolicity coupled to the nonthermal occupation of laser sub-bands.

The reasoning (i) is illustrated in Fig. 7(a), which presents the k-resolved FWHMs for the cases with and without IR-scattering mechanisms included in the calculations.

The former has the dependence, which resembles the one in Fig. 1; with k decreasing, the FWHM initially increases due to the increasing value of the integral in Eq. (2). The expected further increase of the linewidth with decreasing k breaks down at $k^2 \approx 0.2$ nm^{-2}. At this value, the limitation of the non-negative in-plane kinetic energy $E_{\mathbf{k}'} \geq 0$ imposed on the in-scattering states starts to asymmetrize the spectrum and prevents its further broadening. The strength of this effect is especially visible when E_k drops below the FWHM value (approximately equal to

50 meV). As most of the states reside within the energy range described by FWHM, the limitation $E_{\mathbf{k}'} \geq 0$ for the energy of the final state of the scattering event effectively thins their population and makes FWHM decrease. This decrease can be directly observed in Fig. 8, where the energy-momentum position-resolved density of electrons for one module of QCL structure is shown. The bar at $k^2 = 0.1$ nm^{-2} ($E_k = 45$ meV), which measures the upper state width, has the height 50 meV—equal to the FWHM at this k value [see Fig. 7(a)]. A similar bar at $k = 0$ is much shorter. Recall that, for the quantum well analyzed in Sec. II C (see Fig. 1), the decrease of the linewidth in the limit $k \to 0$ is attributed to the IR-scattering mechanism.

In Fig. 7(a), the gap in the data in the range $0.2 < k^2 < 0.3$ nm^{-2} appears due to the highly nonthermal occupation of the laser sub-bands [36–38]. As shown in Fig. 8, the populations in the laser sub-bands are inverted for low-k states and normal for high-k states. Then, either the gain or the absorption arises depending on the k value. For medium k's, there is almost no absorption or gain. It is then hard to estimate the FWHM of the corresponding transitions. However, the lack of FWHM data is of minor relevance. More meaningfull is that—due to the nonparabolicity—the absorption occurs at lower transition energies than the gain. This affects the overall optical spectrum of the upper-to-lower transition. The evolution of the FWHM of the gain spectrum with the increasing number of transitions included in its formation is shown in Fig. 7(b). After the initial increase (resulting from the increasing FWHMs with increasing k's), the FWHM decreases in the region $k^2 > 0.25$ nm^{-2}, in which the inter-sub-band absorption takes place. This effect is observed only when IR scattering is strong enough to make the gain and absorption peaks broad and overlap each other. Then, the resulting peak, being the sum of the two, gets thinner. For IR-free or weak IR scattering, the absorption and gain peaks are narrow, do not overlap, and so the widths of these peaks do not change [see the insets in Fig. 7(b)]. In this case, the theoretical Δ^2 dependence is expected, which is confirmed by the data presented in Fig. 6 inset. As discussed above, the departure from the theoretical dependence observed for larger Δ's is due to the inter-sub-band absorption, which narrows the gain spectrum. For $\Delta = 0.53$ nm, which is the value that best fits the simulations with the experiment, the spectrum is narrowed by $\cong 10$ meV. As a result, the IR part of the total linewidth drops below 50%. This estimate is of some relevance for studies that assume the IR broadening is the only broadening mechanism and identify its parameters from EL or gain spectrum measurements. One example of such a study is the scaling proposed in Ref. [3], which was used to evaluate the dephasing times of various transitions. Our finding indicates that such a procedure may be burdened with considerable uncertainty.

IV. SUMMARY AND CONCLUSIONS

Detailed quantum-mechanical modeling of modern electronic devices allows one to obtain insight into and analyze the processes that otherwise cannot be examined, even with state-of-the-art experimental techniques. Such an analysis, applied to the short-wavelength QCL emitting at approximately 5 μm wavelength reveals that the broadening of the optical linewidth in the range 30–40 meV, typical for this class of devices, is theoretically justified, even if there are no vertical correlations of the interface-roughness potential and the interfaces are not smooth. At room temperature, the IR-scattering contribution to the optical linewidth drops to merely 50%, so the approaches, which rely on the assumption about its almost 100% contribution, can be burdened with substantial numerical uncertainty. The decreased broadening due to IR-scattering is caused by the finite carrier concentration and the decreased population of the final states $\mathbf{k}'$ (which always must fulfill the condition $E_{\mathbf{k}'} \geq 0$) available for the initial state $\mathbf{k}$ in the limit $\mathbf{k} \to 0$. Unlike in other types of devices, e.g., quantum detectors, for which the nonparabolicity is known to increase the broadening [7,56]; in short-wavelength QCLs, the nonparabolicity can lead to line narrowing because of the highly nonthermal occupation of the lower laser sub-band, which destroys the population inversion for the hot carriers.

ACKNOWLEDGMENTS

[1] A. Yariv, *Quantum Electronics,* (Wiley, New York, 1989), 3rd ed.

[2] S. Kumar and Q. Hu, Coherence of resonant-tunneling transport in terahertz quantum cascade lasers, Phys. Rev. B **80**, 245316 (2009).

[3] J. B. Khurgin, Y. Dikmelik, P. Q. Liu, A. J. Hoffman, M. D. Escarra, K. J. Franz, and C. F. Gmachl, Role of interface roughness in the transport and lasing characteristics of quantum-cascade lasers, Appl. Phys. Lett. **94**, 091101 (2009).

[4] T. Ando, Line width of inter-subband absorption in inversion layers: Scattering from charged ions, J. Phys. Soc. Jpn. **54**, 2671 (1985).

[5] K. L. Chapman, H. Schmidt, A. Imamoglu, and A. C. Gossard, Interface roughness and alloy-disorder scattering contributions to intersubband transition linewidths, Appl. Phys. Lett. **69**, 2554 (1996).

[6] T. Unuma, T. Takahashi, T. Noda, M. Yoshita, H. Sakaki, M. Baba, and H. Akiyama, Effects of interface roughness and phonon scattering on intersubband absorption linewidth in a GaAs quantum well, Appl. Phys. Lett. **78,** 3448 (2001).

[7] T. Unuma, M. Yoshita, T. Noda, H. Sakaki, and H. Akiyama, Intersubband absorption linewidth in GaAs quantum wells due to scattering by interface roughness, phonons, alloy disorder, and impurities, J. Appl. Phys. **93,** 1586 (2003).

[8] S. Tsujino, A. Borak, E. Müller, M. Scheinert, C. V. Falub, H. Sigg, D. Grützmacher, M. Giovannini, and J. Faist, Interface-roughness-induced broadening of intersubband electroluminescence in p-SiGe and n-GaInAs/AlInAs quantum-cascade structures, Appl. Phys. Lett. **86**, 062113 (2005).

[9] A. Wittmann, Y. Bonetti, J. Faist, E. Gini, and M. Giovannini, Intersubband linewidths in quantum cascade laser designs, Appl. Phys. Lett. **93**, 141103 (2008).

[10] C. Jirauschek and P. Lugli, Monte-carlo-based spectral gain analysis for terahertz quantum cascade lasers, J. Appl. Phys. **105**, 123102 (2009).

[11] R. Nelander and A. Wacker, Temperature dependence of the gain profile for terahertz quantum cascade lasers, Appl. Phys. Lett. **92**, 081102 (2008).

[12] T. Grange, Contrasting influence of charged impurities on transport and gain in terahertz quantum cascade lasers, Phys. Rev. B **92**, 241306(R) (2015).

[13] K. Wang, T. Grange, T.-T. Lin, L. Wang, Z. Jéhn, S. Birner, J. Yun, W. Terashima, and H. Hirayama, Broadening mechanisms and self-consistent gain calculations for GaN quantum cascade laser structures, Appl. Phys. Lett. **113**, 061109 (2018).

[14] M. Franckié, L. Bosco, M. Beck, C. Bonzon, E. Mavrona, G. Scalari, A. Wacker, and J. Faist, Two-well quantum cascade laser optimization by non-equilibrium green's function modelling, Appl. Phys. Lett. **112**, 021104 (2018).

[15] A. Bismuto, R. Terazzi, M. Beck, and J. Faist, Influence of the growth temperature on the performances of strain-balanced quantum cascade lasers, Appl. Phys. Lett. **98,** 091105 (2011).

[16] D. Botez, J. D. Kirch, C. Boyle, K. M. Oresick, C. Sigler, H. Kim, B. B. Knipfer, J. H. Ryu, D. Lindberg, T. Earles, L. J. Mawst, and Y. V. Flores, High-efficiency, high-power mid-infrared quantum cascade lasers, Opt. Mater. Express **8**, 1378 (2018).

[17] J. Faist, F. Capasso, C. Sirtori, D. L. Sivco, J. N. Baillargeon, A. L. Hutchinson, S. G. Chu, and A. Y. Cho, High power mid-infrared ($\lambda \sim 5$ μm) quantum cascade lasers operating above room temperature, Appl. Phys. Lett. **68**, 3680 (1996).

[18] J. Faist, F. Capasso, D. L. Sivco, A. L. Hutchinson, S.-N. G. Chu, and A. Y. Cho, Short wavelength ($\lambda \sim 3.4$ μm) quantum cascade laser based on strained compensated InGaAs/AlInAs, Appl. Phys. Lett. **72**, 680 (1998).

[19] Y. Bai, S. R. Darvish, S. Slivken, W. Zhang, A. Evans, J. Nguyen, and M. Razeghi, Room temperature continuous wave operation of quantum cascade lasers with watt-level optical power, Appl. Phys. Lett. **92**, 101105 (2008).

[20] A. Lyakh, C. Pflügl, L. Diehl, Q. J. Wang, F. Capasso, X. J. Wang, J. Y. Fan, T. Tanbun-Ek, R. Maulini, A. Tsekoun, R. Go, and C. Kumar N. Patel, 1.6 W high wall plug efficiency, continuous-wave room temperature quantum cascade laser emitting at 4.6μm, Appl. Phys. Lett. **92**, 111110 (2008).

[21] L. V. Keldysh, Diagram technique for nonequilibrium processes, Soviet Phys. JETP **20**, 1018 (1965).

[22] L. Kadanoff and G. Baym, *Quantum Statistical Mechanics: Green's Function Methods in Equilibrium and Nonequilibrium Problems* (Benjamin-Cummings, New York, USA, 1995).

[23] A. Wacker, Gain in quantum cascade lasers and superlattices: A quantum transport theory, Phys. Rev. B **66**, 085326 (2002).

[24] F. Banit, S.-C. Lee, A. Knorr, and A. Wacker, Self-consistent theory of the gain linewidth for quantum-cascade lasers, Appl. Phys. Lett. **86**, 041108 (2005).

[25] I. Waldmüller, J. Förstner, S.-C. Lee, A. Knorr, M. Woerner, K. Reimann, R. A. Kaindl, T. Elsaesser, R. Hey, and K. H. Ploog, Optical dephasing of coherent intersubband transitions in a quasi-two-dimensional electron gas, Phys. Rev. B **69**, 205307 (2004).

[26] A. Matyas, P. Lugli, and C. Jirauschek, Role of collisional broadening in monte carlo simulations of terahertz quantum cascade lasers, Appl. Phys. Lett. **102**, 011101 (2013).

[27] J. Faist, *Quantum Cascade Lasers* (Oxford University Press, Oxford, United Kingdom, 2013), 1.

[28] T. Kubis, C. Yeh, P. Vogl, A. Benz, G. Fasching, and C. Deutsch, Theory of nonequilibrium quantum transport and energy dissipation in terahertz quantum cascade lasers, Phys. Rev. B **79**, 195323 (2009).

[29] R. Lake, G. Klimeck, R. C. Bowen, and D. Jovanovic, Single and multiband modeling of quantum electron transport through layered semiconductor devices, J. Appl. Phys. **81**, 7845 (1997).

[30] C. Jirauschek and T. Kubis, Modeling techniques for quantum cascade lasers, Appl. Phys. Rev. **1**, 011307 (2014).

[31] S.-C. Lee and A. Wacker, Nonequilibrium Green's function theory for transport and gain properties of quantum cascade structures, Phys. Rev. B **66**, 245314 (2002).

[32] A. Y. Song, R. Bhat, P. Bouzi, C.-E. Zah, and C. F. Gmachl, Three-dimensional interface roughness in layered semiconductor structures and its effect on intersubband transitions, Phys. Rev. B **94**, 165307 (2016).

[33] T. Grange, S. Mukherjee, G. Capellini, M. Montanari, L. Persichetti, L. Di Gaspare, S. Birner, A. Attiaoui, O. Moutanabbir, M. Virgilio, and M. De Seta, Atomic-Scale Insights into Semiconductor Heterostructures: From Experimental Three-Dimensional Analysis of the Interface to a Generalized Theory of Interfacial Roughness Scattering, Phys. Rev. Appl. **13**, 044062 (2020).

[34] F. Chevoir and B. Vinter, Scattering-assisted tunneling in double-barrier diodes: Scattering rates and valley current, Phys. Rev. B **47**, 7260 (1993).

[35] M. Franckié, D. O. Winge, J. Wolf, V. Liverini, E. Dupont, V. Trinité, J. Faist, and A. Wacker, Impact of interface roughness distributions on the operation of quantum cascade lasers, Opt. Express **23**, 5201 (2015).

[36] A. Kolek, G. Hałdaś, and M. Bugajski, Nonthermal carrier distributions in the subbands of 2-phonon resonance mid-infrared quantum cascade laser, Appl. Phys. Lett. **101**, 061110 (2012).

[37] O. Jonasson, S. Mei, F. Karimi, J. Kirch, D. Botez, L. Mawst, and I. Knezevic, Quantum transport simulation of

high-power 4.6-μm Quantum cascade lasers, Photonics **3**, 38 (2016).

[38] R. C. Iotti and F. Rossi, Nature of Charge Transport in Quantum-Cascade Lasers, Phys. Rev. Lett. **87**, 146603 (2001).

[39] P. Gutowski, I. Sankowska, P. Karbownik, D. Pierścińska, O. Serebrennikova, M. Morawiec, E. Pruszyńska-Karbownik, K. Gołaszewska-Malec, K. Pierściński, J. Muszalski, and M. Bugajski, MBE growth of strain-compensated InGaAs/InAlAs/InP quantum cascade lasers, J. Cryst. Growth **466**, 22 (2017).

[40] A. Evans, J. Nguyen, S. Slivken, J. S. Yu, S. R. Darvish, and M. Razeghi, Quantum-cascade lasers operating in continuous-wave mode above 90 °C at $\lambda \sim 5.25~\mu$m, Appl. Phys. Lett. **88**, 051105 (2006).

[41] Y. Yao, A. Alfaro-Martinez, K. J. Franz, W. O. Charles, A. Shen, M. C. Tamargo, and C. F. Gmachl, Room temperature and narrow intersubband electroluminescence from ZnCdSe/ZnCdMgSe quantum cascade laser structures, Appl. Phys. Lett. **99**, 041113 (2011).

[42] C. Sirtori, F. Capasso, J. Faist, and S. Scandolo, Nonparabolicity and a sum rule associated with bound-to-bound and bound-to-continuum intersubband transitions in quantum wells, Phys. Rev. B **50**, 8663 (1994).

[43] G. Hałdaś, Implementation of non-uniform mesh in non-equilibrium Green's function simulations of quantum cascade lasers, J. Comput. Electron. **18**, 1400 (2019).

[44] G. Hałdaś, A. Kolek, and I. Tralle, Modeling of mid-infrared quantum cascade laser by means of nonequilibrium green's functions, IEEE J. Quantum Electron. **47**, 878 (2011).

[45] S. Datta, *Electronic Transport in Mesoscopic Systems* (Cambridge University Press, Cambridge, Great Britain, 1995).

[46] T. Kato and S. Souma, Study of an application of nonparabolic complex band structures to the design for mid-infrared quantum cascade lasers, J. Appl. Phys. **125**, 073101 (2019).

[47] C. G. Van de Walle, Band lineups and deformation potentials in the model-solid theory, Phys. Rev. B **39**, 1871 (1989).

[48] I. Vurgaftman, J. R. Meyer, and L. R. Ram-Mohan, Band parameters for III-V compound semiconductors and their alloys, J. Appl. Phys. **89**, 5815 (2001).

[49] T. Kubis, S. R. Mehrotra, and G. Klimeck, Design concepts of terahertz quantum cascade lasers: Proposal for terahertz laser efficiency improvements, Appl. Phys. Lett. **97**, 261106 (2010).

[50] D. Ferry, *Semiconductor Transport* (CRC Press, Boca Raton, FL, USA, 2020), 1.

[51] See Supplemental Material at http://link.aps.org/supplemental/10.1103/PhysRevApplied.17.014019 for more computational details.

[52] A. Kolek, Nonequilibrium Green's function formulation of intersubband absorption for nonparabolic single-band effective mass Hamiltonian, Appl. Phys. Lett. **106**, 181102 (2015).

[53] A. Wacker, M. Franckie, and D. Winge, Nonequilibrium green's function model for simulation of quantum cascade laser devices under operating conditions, IEEE Journal

on Selected Topics in Quantum Electronics **19**, 1200611 (2013).

[54] S. Soleimanikahnoj, O. Jonasson, F. Karimi, and I. Kneze-vic, Numerically efficient density-matrix technique for modeling electronic transport in mid-infrared quantum cas-cade lasers, J. Comput. Electron. **20**, 280 (2021).

[55] M. Lindskog, J. M. Wolf, V. Trinite, V. Liverini, J. Faist, G. Maisons, M. Carras, R. Aidam, R. Ostendorf, and A. Wacker, Comparative analysis of quantum cascade laser modeling based on density matrices and non-equilibrium Green's functions, Appl. Phys. Lett. **105**, 103106 (2014).

[56] V. Gorfinkel, S. Luryi, and B. Gelmont, Theory of gain spectra for quantum cascade lasers and temperature depen-dence of their characteristics at low and moderate car-rier concentrations, IEEE J. Quantum Electron **32**, 1995 (1996).